



# 2<sup>nd</sup> Advanced Optical Metrology Compendium

## Advanced Optical Metrology

Geoscience | Corrosion | Particles | Additive Manufacturing: Metallurgy, Cut Analysis & Porosity



**EVIDENT**  
**OLYMPUS**

**WILEY**

The latest eBook from **Advanced Optical Metrology**.  
Download for free.

This compendium includes a collection of optical metrology papers, a repository of teaching materials, and instructions on how to publish scientific achievements.

With the aim of improving communication between fundamental research and industrial applications in the field of optical metrology we have collected and organized existing information and made it more accessible and useful for researchers and practitioners.

**EVIDENT**  
**OLYMPUS**

**WILEY**

# Electromechanical Behavior of Al/Al<sub>2</sub>O<sub>3</sub> Multilayers on Flexible Substrates: Insights from In Situ Film Stress and Resistance Measurements

Barbara Putz,\* Thomas E.J. Edwards, Emese Huszar, Patric A. Gruber, Kevin-P. Gradwohl, Patrice Kreiml, Daniel M. Többens, and Johann Michler

A series of Al and Al/Al<sub>2</sub>O<sub>3</sub> thin-film multilayer structures on flexible polymer substrates are fabricated with a unique deposition chamber combining magnetron sputtering (Al) and atomic layer deposition (ALD, Al<sub>2</sub>O<sub>3</sub>, nominal thickness 2.4–9.4 nm) without breaking vacuum and thoroughly characterized using transmission electron microscopy (TEM). The electromechanical behavior of the multilayers and Al reference films is investigated in tension with in situ X-ray diffraction (XRD) and four-point probe resistance measurements. All films exhibit excellent interfacial adhesion, with no delamination in the investigated strain range (12%). For the first time, an adhesion-promoting naturally forming amorphous interlayer is confirmed for thin films sputter deposited onto polymers under laboratory conditions. The evolution of Al film stresses and electrical resistance reveal changes in the deformation behavior as a function of oxide thickness. Strengthening of Al is observed with increasing oxide thickness. Significant embrittlement can be avoided for oxide layer thicknesses  $\leq 2.4$  nm.

and optimize mechanical properties. Enhancement in both, multilayer hardness and ductility, is achieved compared to rule of mixture values, depending on the bilayer thickness, the thickness ratio between ceramic and metal layers, and interfacial properties.<sup>[9,13]</sup> For thin layers (>10 nm) the metal can undergo elastic-plastic deformation while the ceramic layer deforms elastically until it fails due to cracking,<sup>[4]</sup> alternatively, highly localized shear deformation may occur as a result of localized stresses at the interfaces.<sup>[5,9,15,17,19]</sup> When the layer thickness is reduced to a few nanometers, ultra-thin ceramics can plastically co-deform with metal layers, as has been demonstrated for Al/TiN.<sup>[4,18]</sup> Substantial intrinsic ductility at small scales has also been demonstrated for amorphous oxides

(40 nm Al<sub>2</sub>O<sub>3</sub>)<sup>[20]</sup> provided that the material is dense and free of geometrical flaws, whereby mechanical characterization remains experimentally challenging.


Metal/ceramic multilayers are of interest for flexible thin-film applications, providing a unique combination of high strength, good conductivity, and potential damage tolerance due to sublayer fragmentation and crack deflection at interfaces. Nanolayered composites of Cu and graphene exhibit a 5–6 times enhanced fatigue resistance compared to the conventional Cu

## 1. Introduction

In recent years, nanoscale metal/ceramic multilayers have come into greater focus as they exhibit promising mechanical, physical, and chemical properties, useful for a wide range of thermal, mechanical, and environmental conditions. Main efforts include manufacturing and characterization<sup>[1–6]</sup> of such structures as well as different experimental<sup>[4,5,7–15]</sup> and modeling<sup>[9,13,16–19]</sup> approaches to understand their deformation mechanisms

B. Putz, T. E. J. Edwards, E. Huszar, J. Michler  
Laboratory for Mechanics of Materials and Nanostructures  
Empa, Swiss Federal Laboratories for Materials Science and Technology  
3602 Thun, Switzerland  
E-mail: barbara.putz@unileoben.ac.at

B. Putz  
Department of Materials Science  
Montanuniversität Leoben  
8700 Leoben, Austria

 The ORCID identification number(s) for the author(s) of this article can be found under <https://doi.org/10.1002/adem.202200951>.

© 2022 The Authors. Advanced Engineering Materials published by Wiley-VCH GmbH. This is an open access article under the terms of the Creative Commons Attribution License, which permits use, distribution and reproduction in any medium, provided the original work is properly cited.

DOI: 10.1002/adem.202200951

P. A. Gruber  
Karlsruhe Institute of Technology  
Institute for Applied Materials IAM–MMI  
76131 Karlsruhe, Germany

K.-P. Gradwohl  
Leibniz Institut für Kristallzüchtung  
12489 Berlin, Germany

P. Kreiml  
Erich Schmid Institute of Materials Science  
Austrian Academy of Sciences  
8700 Leoben, Austria

D. M. Többens  
Helmholtz–Zentrum Berlin für Materialien und Energie  
12489 Berlin, Germany

thin film in cyclic bending experiments.<sup>[21]</sup> The use of flexible polymer substrates additionally holds advantages in terms of easier sample handling and facilitated the mechanical characterization of extremely thin layers.

This work uses a unique deposition approach combining atomic layer deposition (ALD) and physical vapor deposition (PVD, magnetron sputtering) to fabricate multilayer films of crystalline Al and amorphous Al<sub>2</sub>O<sub>3</sub> on flexible polyimide substrates. An advantage of combining the metal layer with its natural oxide is excellent adhesion between the individual layers, reducing of the risk of spontaneous delamination, and ensuring the structural integrity of the multilayer system.<sup>[22]</sup> Compared to pulsed gas electron beam deposition,<sup>[23]</sup> the combined ALD/PVD approach allows for the deposition of stoichiometric amorphous oxide layers with sub-nm precision well below the native oxide thickness of pure Al films (2–10 nm<sup>[24]</sup>), however, at lower deposition rates. Indeed, in the study by Alpas et al.,<sup>[23]</sup> Al/Al<sub>2</sub>O<sub>3</sub> multilayers totaling 25 μm thickness employed natural oxidation resulting in oxide layer thicknesses of about 5 nm and further control of oxide thickness required co-sputtering from an Al<sub>2</sub>O<sub>3</sub> target to achieve thicker oxide layers.<sup>[25]</sup> Amorphous ALD oxide (Al<sub>2</sub>O<sub>3</sub>) layers have the possibility of improved intrinsic ductility by optimization of process parameters, while Al is vital for both fundamental and industrial purposes.

It is known that the deformation behavior of flexible multilayer structures is often dominated by the most brittle component with a drastic impact on application-relevant mechanical and functional properties. Cracks in the brittle layers cause stress concentration and fracture of ductile layers at very low strains (1–2%).<sup>[26–29]</sup> Embrittlement depends on the modulation period  $\lambda = t_{\text{brittle}} + t_{\text{ductile}}$  and modulation ratio  $\eta = t_{\text{brittle}}/t_{\text{ductile}}$ ,<sup>[30]</sup> where  $t$  is equal to the film thickness; ductile deformation is preserved in a small parameter region with  $\eta < 0.2$ . The outstanding oxide thickness control of ALD, and the ability to operate ALD/PVD deposition without breaking vacuum opens up a wide range of novel, otherwise unachievable modulation and thickness ratios for Al/Al<sub>2</sub>O<sub>3</sub> multilayers. Ultrathin oxide layers can confine the grain growth of the metallic films, creating an Al sublayer structure for improved mechanical performance and damage tolerance without embrittlement.

Damage tolerance and mechanical behavior of flexible thin films are well reflected in in situ X-ray diffraction (XRD) combined with electrical resistance measurements and post-mortem fragmentation analysis. Common setups include uni<sup>[26,31–33]</sup> and biaxial tensile loading.<sup>[34–37]</sup> Film stress evolution parallel and perpendicular to the tensile direction give information on the different deformation mechanisms in crystalline layers. The electrical resistance yields information from the entire thin film and is extremely sensitive to the formation of through-thickness cracks or a critical crack density<sup>[38]</sup> perpendicular to the current direction in brittle and ductile films, respectively. Even information on crack length, width, and spacing can be extracted from in situ resistance data.<sup>[39,40]</sup> Additionally, conclusions about oxide layer fracture can be drawn via the known embrittlement effects. It will be demonstrated that the damage tolerance of Al/Al<sub>2</sub>O<sub>3</sub> multilayers on polymers under uniaxial tensile loading can be improved significantly as a function of decreasing oxide layer thickness. We will also contextualize the beneficial deformation behavior of our metal/oxide films

and the impact of PVD/ALD deposition relative to length-scale dependent deformation of the more established PVD/PVD brittle–ductile multilayer systems on flexible polymers. The ability to engineer metallic thin films with sublayer structures and grain sizes well below the total film thickness without embrittlement opens up new possibilities for the design of damage-tolerant thin films with a unique property profile for future flexible and rigid thin-film applications.

## 2. Results

### 2.1. Structural Characterization

To evaluate the electromechanical fragmentation behavior of Al-based multilayers as a function of embedded oxide layer thickness, three Al/Al<sub>2</sub>O<sub>3</sub> multilayers were fabricated using combined PVD/ALD deposition: 50/9.4/50/9.4/50, 50/2.4/50/2.4/50, 50/1cycle/50/1cycle/50 (thickness in nm), along with 50 nm and 150 nm Al reference films. The multilayer systems are referred to as 50/9.4, 50/2.4, and 50/1cycle, respectively, throughout the manuscript. Typically, a single ALD cycle on metal surfaces does not result in a continuous monolayer with full surface coverage.<sup>[41,42]</sup> Therefore, rather than fabricating a continuous oxide film, the purpose of one single, full ALD cycle (nominal thickness 0.14 nm Al<sub>2</sub>O<sub>3</sub> based on average growth per cycle (GPC)) is to interrupt the Al microstructure in a controlled manner and produce 150 nm Al samples with a 50 nm sublayer architecture. Overview and high-resolution transmission electron microscopy (HR-TEM) cross-sections of the fabricated reference and multilayer thin films are shown in **Figure 1**. While the exemplary micrographs are on Si substrates, similar microstructures were obtained on polyimide (**Figure 2a**). The 150 and 50 nm Al reference films (**Figure 1a,b**) exhibit a homogeneous film thickness and columnar grains. The average in-plane grain size and standard deviation were measured from cross-sectional TEM images as  $97 \pm 31$  and  $42 \pm 14$  nm, for 150 and 50 nm films, respectively. All Al sublayers in the multilayers (**Figure 1c–e**) also exhibit a homogeneous film thickness with columnar grains constrained by the intermediate amorphous Al<sub>2</sub>O<sub>3</sub> layers and similar average in-plane grain sizes determined as  $56 \pm 22$  nm (50/1cycle),  $54 \pm 20$  nm (50/2.4) and  $42 \pm 18$  nm (50/9.4). Grain size and oxide layer thickness values are summarized in the Supporting Information (**Figure S1**, Supporting Information). The thicker oxides (**Figure 1d,e**) are visible as continuous, homogeneous bands. Noteworthy is that, as evident from **Figure 1c**, even a single cycle of ALD is sufficient to interrupt Al grain growth and leads to a re-nucleation of Al grains, resulting in an Al sublayer architecture. Corresponding high-resolution TEM images of the Al<sub>2</sub>O<sub>3</sub> layers are shown in **Figure 1f,h**. For the thicker oxides, layer thicknesses were measured from TEM cross-sections as  $3.2 \pm 0.2$  and  $9.3 \pm 0.3$  nm. Based on the reported GPC of Al<sub>2</sub>O<sub>3</sub> (0.14 nm) thicknesses of 2.4 and 9.4 nm are expected for 17 and 67 cycles, respectively. It is important to consider the limitations of accurate thickness measurements from cross-sectional imaging at such small scales which can lead to overestimation, as discussed further in the discussion. For the single ALD cycle sample, the determination of oxide thickness from TEM cross-sections is not possible.



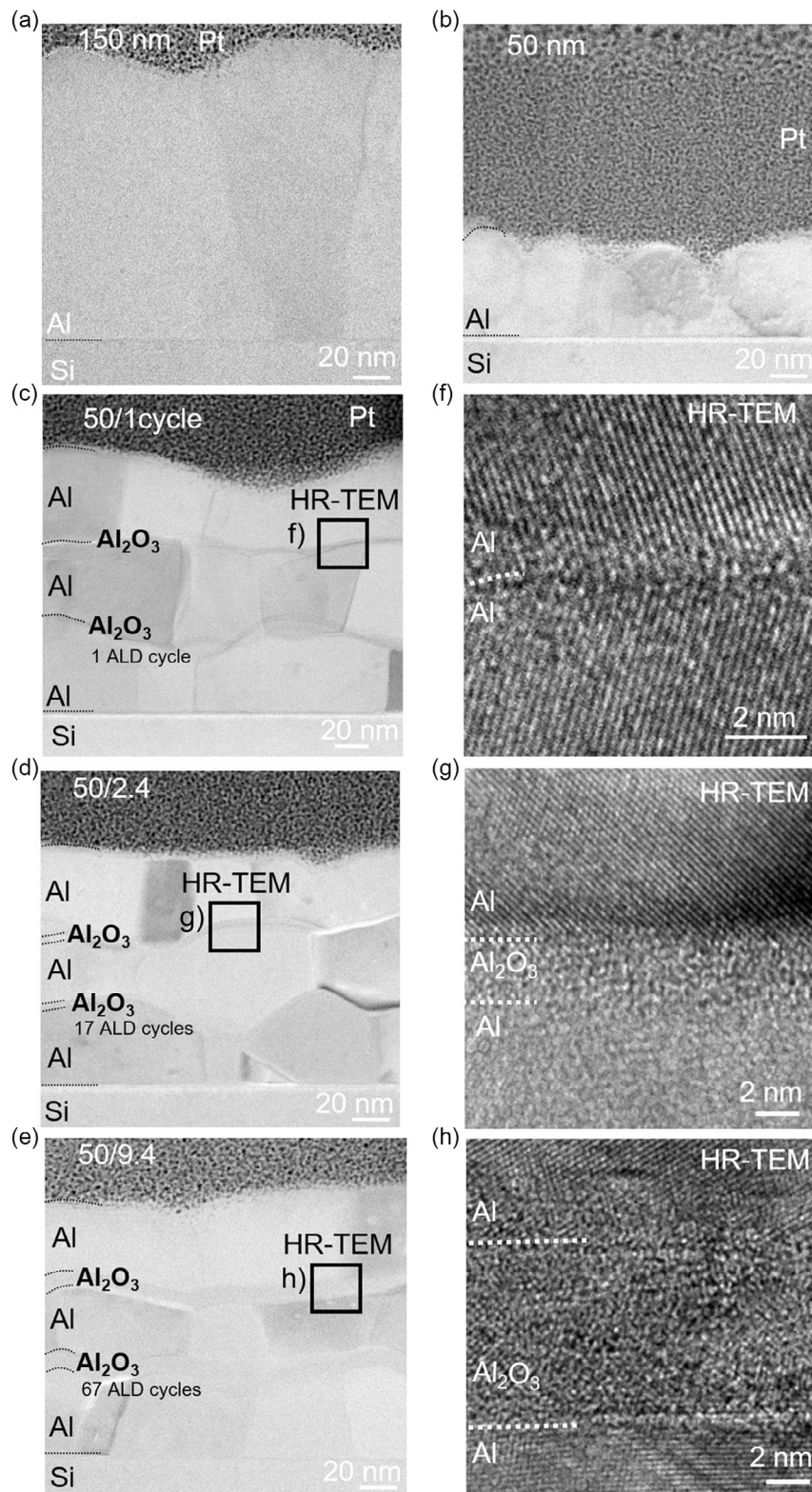


**Figure 1.** Transmission electron microscopy (TEM) cross-sections of the investigated thin-film systems. a) 150 nm; and b) 50 nm Al reference samples with columnar grains of the order of the film thickness; c–e) Multilayers exhibiting 50 nm Al sub-layers, whose columnar microstructure is constrained by intermediate amorphous Al<sub>2</sub>O<sub>3</sub> layers of increasing thickness (nominally 0.14–9.4 nm); f–h) Corresponding high-resolution TEM (HR-TEM) images of two adjacent Al sublayers separated by amorphous Al<sub>2</sub>O<sub>3</sub>. Please note the different magnification in (f).

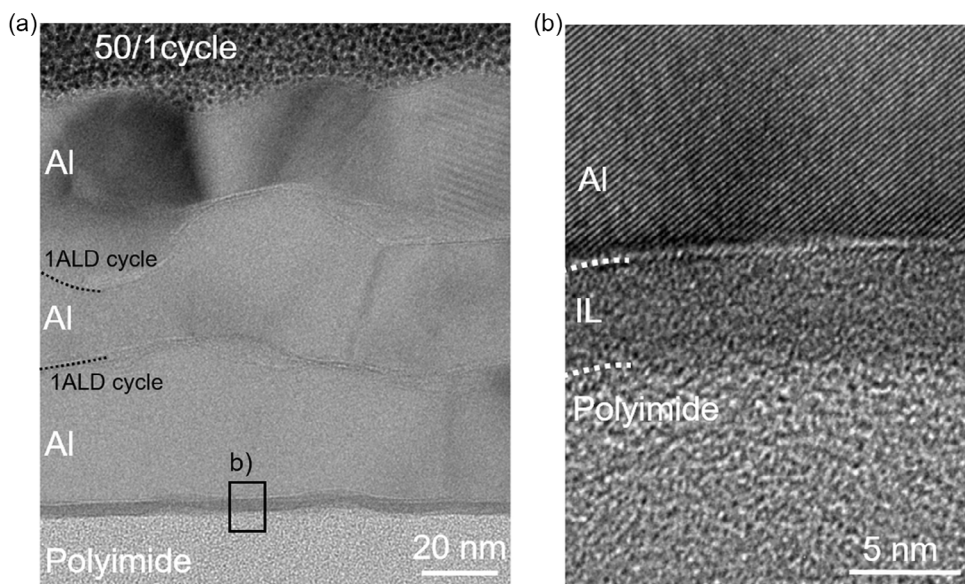


**Figure 2.** TEM cross-sections of thin films on polymer substrate. a) Overview and b) HR-TEM analysis of the 50/1 cycle multilayer on polyimide. An amorphous interlayer (IL) formed during sputter deposition of the first Al layer at the interface between polyimide and Al.

However, the HR-TEM micrograph (Figure 1f) shows a distinct but very narrow interface between two adjacent Al sublayers, with atom rows of adjacent Al layers convening without interruption at the single-cycle ALD layer.

Figure 2 shows overview and high-resolution TEM cross-sections of the single-cycle ALD 50/1 cycle multilayer stack on polyimide. Besides the structure specific to the metal–polymer interface (Figure 2b), the multilayer structures obtained on polyimide (Figure 2a) and Si substrates are similar (Figure 1). At the metal–polymer interface, a homogeneous interlayer (IL) is observed, which forms between PI and Al during sputter deposition of the first Al layer. The thickness of this interlayer was measured from cross-sectional TEM images as  $5.2 \pm 0.2$  nm.

## 2.2. Mechanical Characterization

The electromechanical behavior of the different multilayer structures as a function of oxide layer thickness is summarized in Figure 3, including a schematic of the experimental setup. One representative sample is shown for each system together with a pure 50 and 150 nm Al reference film. From the longitudinal film stress evolution (parallel to straining direction, 111 Al Bragg peak) mechanical deformation characteristics of Al, equivalent to yield or fracture stresses can be extracted. The measured signal is an average of the three Al sublayers, since the method is unable to resolve individual layers of the same material in the film thickness direction. Due to the amorphous nature and small thickness of the  $\text{Al}_2\text{O}_3$  layers, no XRD signal could be obtained. Additionally, the normalized resistance  $R/R_0$  (initial resistance  $R_0$ ) is highly sensitive to irregularities in the film and indicates electrical degradation and failure of the thin films. Upon loading,  $R/R_0$  increases as a result of changing sample dimension according to the relation  $R/R_0 = (L/L_0)^2 \equiv (1 + \epsilon^2)$  (constant volume approximation, gauge length  $L$ , initial length  $L_0$ ).<sup>[43]</sup> This theoretical increase is included in Figure 3 as dashed green lines.

Substantial strain-induced structural modifications of the film, such as necks or through-thickness cracks, yield an increase and deviation of the resistance ratio from the theoretical curve. In accordance with the literature, electrical failure is defined as a 10% deviation from the constant volume approximation (pink dashed line).<sup>[44]</sup> Any noise in the recorded resistance data (Figure 3c) is an experimental artifact from stage tilting and not a characteristic of thin-film deformation.

The 150 nm Al reference sample (Figure 3a, top) exhibits fairly ductile deformation and resistance behavior in the longitudinal direction. Upon loading the longitudinal film stress increases linearly, until the elastic limit is reached around 1.5% applied strain. After reaching the maximum stress ( $\approx 300$  MPa), the film stress plateaus at an almost constant value with little stress relaxation upon further loading within the applied strain range. In comparison, perfectly ductile thin films would not experience any stress relaxation after reaching the maximum stress.<sup>[45,46]</sup> During unloading, compressive stresses build up in the thin film, as a result of purely elastic recovery of the polymer substrate. After an initial stress drop, related to load reversal after the hold period of 3 min, the stress increase is linear, indicating elastic deformation. Compared to initial elastic loading, the slope is slightly reduced, indicating the presence of cracks. The normalized resistance  $R/R_0$  approximately follows the theoretically predicted increase (green dashed line, Figure 3a) during loading up to 6% applied strain. Electrical failure (10% deviation from theory line), due to a sufficient density of tensile-induced cracks, is observed around 10% strain. At the maximum applied strain (12%) a 20% resistance deviation compared to a defect-free reference is observed. Upon unloading, the resistance ratio recovers linearly (slope approximately parallel to the theory line), yielding a final resistance ratio of 1.3. The thinner 50 nm Al reference sample exhibits a ductile-like electromechanical behavior in the longitudinal direction (Figure 3b, top). Due to a weaker XRD signal, there is a bigger scatter in the film stress data,

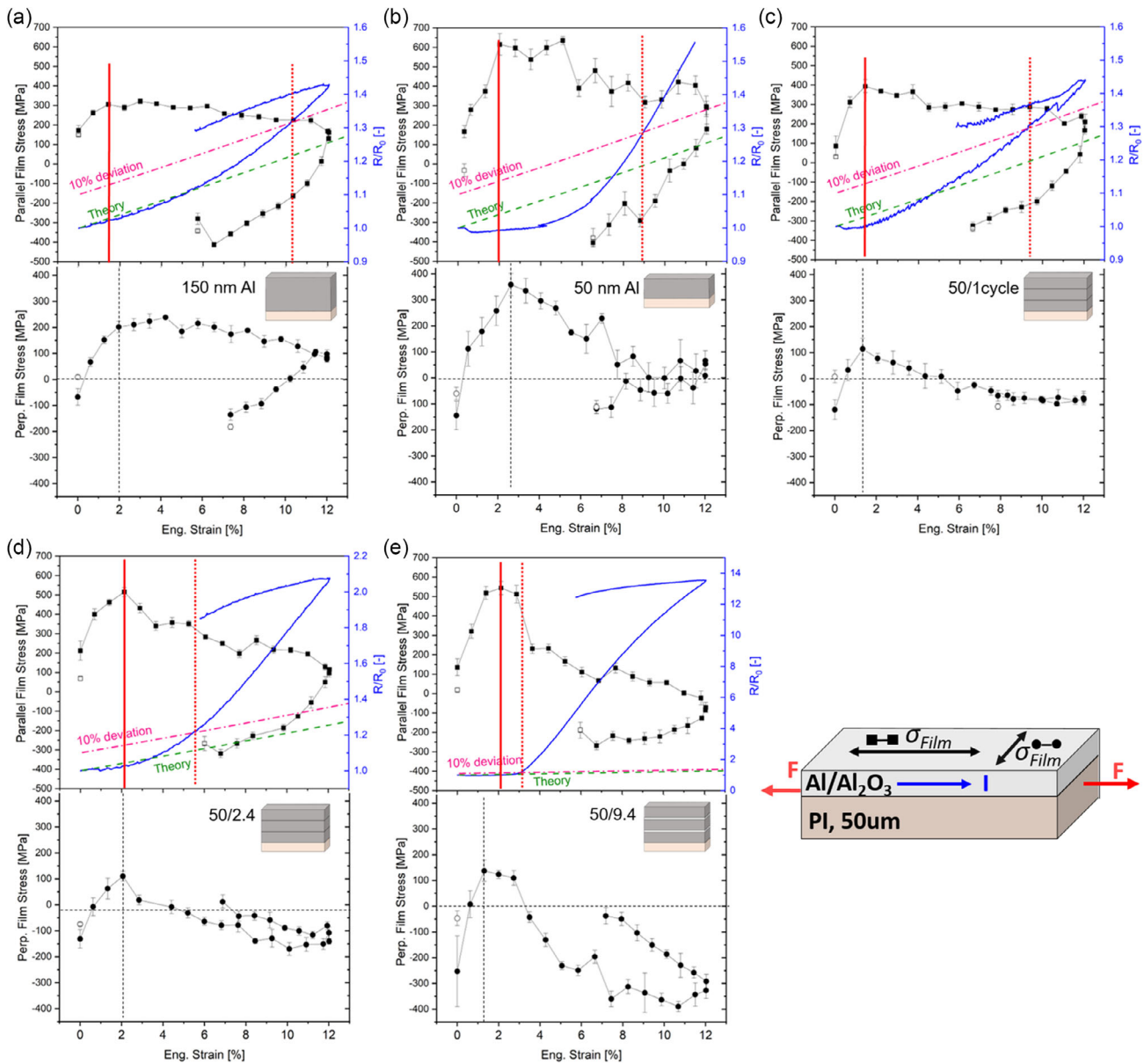


**Figure 3.** Evolution of Al film stresses parallel (top) and perpendicular (bottom) to the straining direction and relative resistance ratios (blue) as a function of applied strain. a) 150 nm Al; b) 50 nm Al; c) 50/1cycle; d) 50/2.4; e) 50/9.4. The standard deviation is used to calculate the error bars. The theoretical resistance increase and 10% deviation thereof are indicated with green and pink dashed lines. Mechanical and electrical failure are indicated with continuous and dotted vertical red lines, respectively. Please also note the different scale for  $R/R_0$  in (d) and (e). Lower right: Schematic of the experimental setup.

exacerbating an unambiguous interpretation of the film stress evolution. The maximum stress ( $\approx 600$  MPa) is reached at 2% applied strain, followed by a stress decrease and electrical failure around 9% applied strain. In the initial loading section, the resistance ratio shows a substantial drop below the theory line, which is (to a varying extent) present in all investigated samples due to contacting in the experimental setup and will be discussed separately. The unloading segment of the resistance curve was lost due to experimental challenges.

For the multilayer samples, a gradual strengthening and embrittlement is observed with increasing oxide layer thickness. The 50/1cycle Al film, where sublayers are interrupted by 1  $\text{Al}_2\text{O}_3$

ALD cycle (Figure 3c, top) still exhibits ductile-like behavior. The shape of the stress–strain curve is similar to the 150 nm Al reference sample. The maximum stress ( $\approx 400$  MPa) is followed by a stress plateau with a small drop of around 4%. The total amount of stress decrease within the applied strain range is similar to the 150 nm Al film. Electrical failure is observed around 9% applied strain and the resistance ratio at maximum strain is identical to the 150 nm film. Noise in the resistance signal and the sudden drop of around 11% stem from instrumentation and are no characteristics of film deformation. The unloading behavior is similar to the reference samples in terms of compressive stress evolution and resistance recovery. In contrast, the Al film stress evolution



with 2.4 nm oxide layers (Figure 3d, top) exhibits a stress peak ( $\approx 500$  MPa) during loading at 2% strain followed by an immediate stress relaxation and a stress plateau. Stress relaxation is typically due to cracking, where cracks locally relax the stresses along their edges, leading to a pronounced decrease in the average stress measured in the film. A similar stress evolution is observed with 9.4 nm oxides (Figure 3e, top), whereby the stress relaxation (peak stress  $\approx 550$  MPa around 2%) is more pronounced (total relaxation to zero film stress), indicating more extensive through-layer or through-thickness cracking.

The varying extent of embrittlement is also well reflected in the resistance curves. The 50/1cycle film shows a resistance behavior comparable to the reference samples (failure strain 9 and 10%). With 2.4 nm oxides, electrical failure around 5.5% is followed by a moderate resistance increase, where the resistance ratios at the maximum applied strain and after unloading,  $(R/R_0)_{\max}$  and  $(R/R_0)_{\text{End}}$ , respectively, are 40–50% higher as compared to the ductile samples. With 9.4 nm oxide layers, electrical failure is shifted down to 3% applied strain and the resistance increase within the applied strain range is 10 times higher than the reference samples' resistance increase. Readers should note the different scales for the normalized resistance curves in Figure 3d,e. Rapid resistance increase is related to extensive through-thickness crack formation severely disrupting the flow of electric current through the Al layers. A high value of  $R/R_0$  after unloading indicates that the generated through-thickness cracks remain open despite the elastic relaxation of the polymer.

The film stresses in the transverse direction (perpendicular to the straining direction, Figure 3a–e, bottom) initially increase like in the parallel direction, due to a slight mismatch of the different Poisson's ratios of the film and the substrate.<sup>[45,47,48]</sup> Only the 150 nm Al film (Figure 3a, bottom) shows ductile behavior with a film stress evolution similar to the parallel direction (elastic regime, plateau, compressive during unloading). For all multilayer films and the 50 nm Al reference, a peak is observed

in transverse film stress. The peak position corresponds well to cracking in the longitudinal direction, indicating a good correlation between the two datasets. Similar to the longitudinal case, the maximum stress value  $\sigma_{\max, \text{trans}}$  increases with increasing oxide thickness. Upon further loading, film stresses in the transverse direction relax and even become progressively compressive in the case of thicker oxide layers (Figure 3d,e, bottom). This build-up of substantial compressive stresses during loading can result in local delamination (buckling) of the films, if their magnitude exceeds the interfacial adhesion energy. Buckling would result in a relaxation of compressive stresses during loading,<sup>[47]</sup> which is not observed within the investigated strain range, attesting good adhesion to the fabricated multilayers. Instead, the accumulated compressive stresses only decrease during unloading.

### 2.3. Post-Mortem SEM Characterization

Post-mortem SEM characterization of the sample surface after tensile straining is summarized in Figure 4. For the 150 nm Al reference sample (Figure 4a) an increased surface roughness is observed as compared to the 50 nm Al film (Figure 4b) and the multilayer coatings (Figure 4c–e). There is a good correlation between the combined XRD and resistance data, and the observed tensile-induced crack formation. Up to an oxide thickness of 2.4 nm (Figure 4c,d) the tensile-induced crack pattern is comparable to the ductile Al reference films. Discontinuous short cracks, indicated by white arrows, are visible on the surface, particularly at higher magnifications (insets Figure 4a–d). All insets are the same size ( $1.8 \mu\text{m} \times 2.2 \mu\text{m}$ ) to facilitate comparison. The crack spacing (distance between two cracks) of the ductile multilayers (Figure 4c, d) is similar to the 50 nm Al reference film (Figure 4b,  $\approx 3$  cracks per inset). As expected, the crack spacing of the thicker 150 nm Al film (Figure 4a) is slightly larger (2 cracks per inset).

With 9.4 nm oxide thickness, the observed crack pattern changes significantly, showing continuous, long straight cracks.

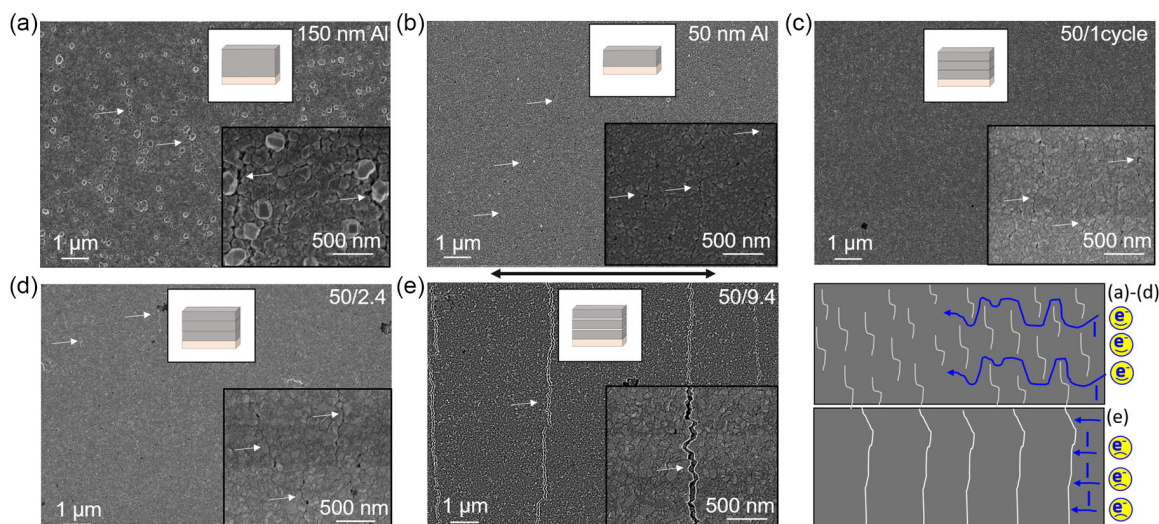


**Figure 4.** Post-mortem scanning electron microscopy (SEM) characterization of the samples after uniaxial loading to 12% strain. Discontinuous, short cracks are visible for the ductile: a) 150 nm Al and b) 50 nm Al sample, and c, d) up to an oxide thickness of 2.4 nm. e) Long, straight, and open cracks are visible for multilayers of 50 nm Al and 9.4 nm  $\text{Al}_2\text{O}_3$ . Cracks are indicated with white arrows. The tensile axis is horizontal, as indicated by the black arrow. Lower right: Schematic representation of the crack patterns with discontinuous short or long cracks, posing obstacles for the flow of electric current.

The spacing between these cracks is larger than for the ductile samples (only 1 crack per insert image, Figure 4e) and was determined as  $3.23 \pm 1.00 \mu\text{m}$  from SEM images. Even after unloading and time-dependent relaxation of the polymer substrate, the cracks remain open, corresponding to the high final resistance ratio  $(R/R_0)_{\text{End}}$ . For the ductile samples, particularly multilayers, cracks appear more closed with contacting crack edges. In general, ductile crack patterns are electrically more favorable, allowing electrons to pass between discontinuous short cracks, as indicated schematically in Figure 4 (bottom right). All samples have been strained to the same maximum strain level of 12%. In agreement with the perpendicular film stress evolution (Figure 3), no tensile-induced delamination (buckles) was observed on either of the film surfaces.

Focused ion beam (FIB) cross-sections (Figure 5) reveal the film damage in the thickness direction, with a variety of different crack morphologies. Dashed white circles and arrows indicate cracks visible in the cross-section. For the reference Al films (Figure 5a,b), cracks visible on the surface penetrate the entire film thickness. For the multilayer samples, the Al sublayer structure can be resolved (Figure 1c–e). Interestingly, not all cracks are through-thickness, despite a maximum applied strain of 12%. Rather, some cracks start and are constrained to either the bottom or bottom and top layers, while the middle Al sublayer remains intact. This is observed even for the long and straight cracks with 9.4 nm oxide thickness (Figure 1e), of which some are not extending through the entire sample thickness.

Statistical analysis of cross-sectional crack propagation is difficult due to exacerbated imaging and low film thickness.

### 3. Discussion

#### 3.1. Oxide Layer Thickness

Cross-sectional characterization of the multilayers revealed a small discrepancy between nominal and measured oxide layer thicknesses at low ALD cycle numbers. The measured thickness values ( $3.2 \pm 0.2$  and  $9.3 \pm 0.3$  nm) are slightly higher than calculations would predict (2.4 and 9.4 nm) based on the GPC rate reported for  $\text{Al}_2\text{O}_3$  under similar process conditions (0.14 nm, ellipsometry measurements<sup>[6]</sup>). This could indicate the presence of a native oxide layer on the order of 1 nm prior to the first ALD cycle, despite the fact that sample transfer was performed without breaking vacuum. For the self-same ALD/PVD sputter system and identical growth conditions used in this study, Xie et al. report linearly increasing thicknesses of  $\text{Al}_2\text{O}_3$  layers (1–10 nm) with increasing ALD cycle numbers, suggesting that the deposition system can effectively inhibit native oxidation of aluminum and precisely control the thickness of  $\text{Al}_2\text{O}_3$ .<sup>[6]</sup> The entire transfer procedure from the PVD to the ALD chamber via the load-lock is completed within 5 min (300 s) and throughout the process, the sample is continuously in a high vacuum environment (less than  $1 \times 10^{-4}$  Pa) to avoid self-oxidation of the Al layers.<sup>[6]</sup> A comparison to literature data allows estimating

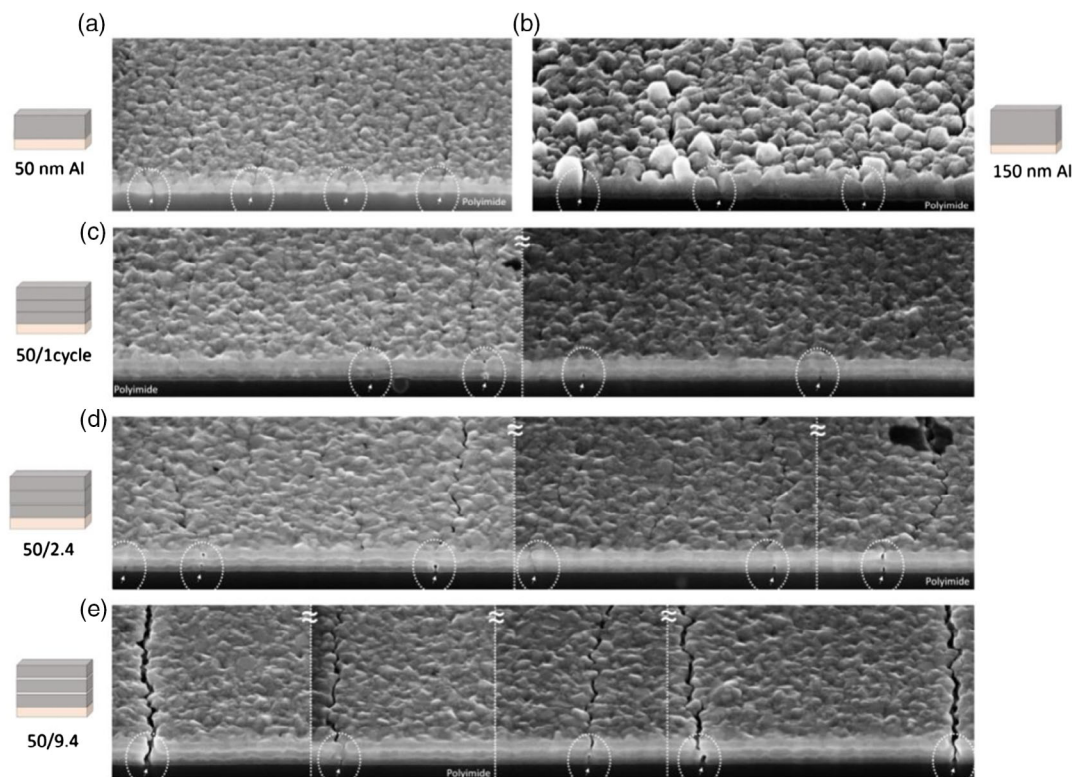


**Figure 5.** Cross-sectional analysis of the crack morphology for the different reference and multilayer systems after unloading. Despite a maximum applied strain of 12% not all cracks penetrate the entire film thickness, with individual sublayers failing and adjacent ones remaining intact. Cracks visible in the cross-section are indicated with white arrows and dashed circles.



the thickness of the natural oxide potentially forming during this transfer process. Jeurgens et al. report a steady-state oxide thickness of approximately 0.4 nm after 300 s at 100 °C and with a partial oxygen pressure of  $1.33 \times 10^{-4}$  Pa.<sup>[49]</sup> The reported conditions are a fairly good representation of the PVD–ALD transfer process, considering the thermal environment in the ALD chamber ( $T_{\text{max}}$  120 °C) and assuming that the partial oxygen pressure equals the total pressure in the chamber ( $<1 \times 10^{-4}$  Pa, conservative estimation yielding the upper limit of the real oxygen concentration). It can therefore be concluded that a parasitic natural oxide layer potentially forming during the transfer would have a maximum thickness of 0.4 nm or less. Such a parasitic layer would have a larger percentile influence on total film thickness and GPC rate at low ALD cycle numbers, thus explaining the increased GPC at 17 cycles ( $0.19 \pm 0.02$  nm), as compared to 67 cycles ( $0.14 \pm 0.003$  nm) which is within the error of reported TEM based GPC rates of  $\text{Al}_2\text{O}_3$  ( $0.14 \pm 0.02$  nm<sup>[6]</sup>). In the same way, extremely thin native oxides can go unnoticed when calculating GPC rates from thick ( $>100$  cycles) ALD layers, unless low cycle numbers are investigated simultaneously with in situ ellipsometry.<sup>[50]</sup>

In contrast, the high-resolution TEM micrograph of the single  $\text{Al}_2\text{O}_3$  ALD cycle (Figure 1f) attests a distinct but very narrow interface between two adjacent Al sublayers, with atom rows of adjacent Al layers convening without interruption at the single-cycle ALD layer. This further enhances the authors' confidence that no oxidation occurs during the PVD–ALD transfer and that the increased oxide thickness at 17 cycles is mainly due to the thickness measurement method from cross-sectional TEM lamellae. While it remains the only way of determining the thickness of the oxides incorporated in multilayers, the method tends to overestimate the layer thickness, and so the limits of measuring thickness and calculating GPC rates from TEM cross-sections need to be discussed. One source of error originates from the difficulty of clearly defining the boundaries between amorphous and crystalline layers from the presented HR-TEM micrographs (Figure 1), particularly for ultra-thin oxide layers. More fundamentally, TEM lamellae will only show true thickness values if the beam direction is perfectly parallel to the multilayer interfaces. Any tilt due to the 3D shape of the outer surface of individual Al grains results in an increased apparent oxide thickness and only the smallest measured values should therefore be considered closest to the actual thickness. The magnitude of this overestimation is a function of the angle between the actual and the perfect beam-parallel orientation of the interface. From the TEM images in Figure 1c–e, the maximum deviation from the horizontal of the top surface of an Al sublayer was measured as 30° for both oxide thicknesses. Using this value as a first approximation, an oxide tilt angle of 30° relative to perfect in-plane alignment can yield a phantom thickness increase of about 15%.

Regarding the oxide layer in the 50/1cycle sample (Figure 1c,f), in situ scanning tunneling spectroscopy experiments probing the growth mechanisms and physical properties of ALD  $\text{Al}_2\text{O}_3$  on Al substrates after vacuum transfer show that a single cycle does not result in a continuous monolayer.<sup>[41]</sup> Depending on the length of an initial  $\text{H}_2\text{O}$  pulse ( $1\text{--}3$  s<sup>[41]</sup>), which supports the creation of an atomically thin uniform oxide layer, and the deposition temperature ( $60\text{--}225$  °C<sup>[42]</sup>) the surface coverage after one single ALD cycle on Al is between 54% and 93%. Since our single-cycle ALD deposition is performed without an initial  $\text{H}_2\text{O}$  pulse, we do not expect

our resulting  $\text{Al}_2\text{O}_3$  monolayer to be continuous either. Still, the ALD surface coverage on the Al surface is interrupting the grain growth for the subsequent sputtering of the Al layers, with no local differences in sublayer grain size.

### 3.2. Interface Structure—Adhesion

It is known that the electromechanical behavior of flexible thin-film systems is influenced by the metal–polymer interface. During sputter deposition of the first Al layer, a homogeneous interlayer (thickness  $\approx 5$  nm) is formed between PI and Al (Figure 2). Such interlayers have been previously reported in the literature for evaporated Ti and Al thin films<sup>[51–53]</sup> on polyimide and polymer layers spin-coated onto Al,<sup>[54]</sup> and are associated with high interfacial quality (good adhesion). However, the influence of the deposition method on metal–polymer interface structure is widely unknown. Notably, this is the first time we can report and confirm the formation of a natural interlayer for thin films sputter deposited under laboratory conditions. Even though no quantitative adhesion analysis has been performed, the absence of tensile-induced delamination (buckling,<sup>[55]</sup> Figure 4), despite the evolution of significant compressive stresses in the transverse direction<sup>[56]</sup> (Figure 3d,e), attests high interfacial quality of all investigated sputter-deposited film systems.

Natural interlayers typically exhibit an amorphous microstructure after deposition.<sup>[51,52]</sup> Their formation is attributed to chemical reactions between carbonyl groups (C=O) of the polymer substrate and arriving metal atoms.<sup>[57]</sup> Subsequent thermal treatments can influence the microstructure<sup>[51]</sup> and thickness<sup>[53]</sup> of the interlayer and deteriorate the adhesive properties of the film. Interlayer crystallization during annealing causes decreased adhesion values and a change in the crack pattern for Ti on PI<sup>[51]</sup>. For evaporated Al on PI small mutations in the interface chemistry and structure were identified after annealing at 225 °C for 140 h.<sup>[53]</sup> Based on the high-resolution TEM imaging (Figure 2b), the observed crack patterns (Figure 4) and good interface quality of our multilayers, it can be concluded that the annealing treatments during ALD deposition (120 °C, max 4 h) did not induce crystallization of the amorphous interlayer.

### 3.3. Electrical Behavior—Resistance Evolution during Straining

#### 3.3.1. Resistance of Unstrained Films

The initial resistance values,  $R_0$ , of the unstrained films are listed in Table 1. For the reference Al films, we observe an expected increase in  $R_0$  for decreasing film thickness between 50 nm and 150 nm Al. The initial resistance of the multilayers ( $\approx 1.5$  Ω) is closer to the 150 nm Al (1.3 Ω) reference sample. This is reasonable, as the sampled length and width remained constant for each sample and only the film thickness changed in the nm regime through the addition of the oxide layers. Introducing the  $\text{Al}_2\text{O}_3$  oxide layers seems to not significantly deteriorate the electrical properties of the films. However, the in situ 4PP resistance setup incorporated into the tensile grips is an imperfect way of measuring absolute electrical resistance values of multilayers, as the multilayer architecture is likely to be damaged in the course of clamping the sample firmly to avoid

**Table 1.** Electromechanical properties as a function of thin film architecture. For the multilayer films, the reported maximum stress and initial resistance values are averaged over multiple samples. Where the deviation between individual tests is higher than the error of a single measurement, the standard deviation of those measured values is reported. *N* is the number of repeats of a given thin-film architecture.

	Reference Al films			Al/Al <sub>2</sub> O <sub>3</sub> multilayers	
	50	150	50/1 cycle	50/2.4	50/9.4
Al/Al <sub>2</sub> O <sub>3</sub> [nm]	50	150	50/1 cycle	50/2.4	50/9.4
$\sigma_{\max}$ [MPa]	$\approx 560 \pm 56$	$305 \pm 10$	$360 \pm 47$	$504 \pm 15$	$516 \pm 40$
$\epsilon$ @ $\sigma_{\max}$ [%]	2	1.5	1.5	2	2
$\epsilon_{\text{Res-10\%}}$ [%]	8.9	$10.9 \pm 0.85$	$8.15 \pm 1.5$	$5.47 \pm 0.40$	$2.90 \pm 0.28$
$R/R_0$ max	1.56	$1.41 \pm 0.04$	$1.53 \pm 0.13$	$2.17 \pm 0.13$	$13.0 \pm 0.7$
$R_0$ [Ohm]	$4.95 \pm 0.003^{\text{a}}$	$1.3 \pm 0.06$	$1.59 \pm 0.01$	$1.51 \pm 0.08$	$1.48 \pm 0.06$
$\sigma_{\max, \text{trans}}$ [MPa]	$358 \pm 44$	$239 \pm 6$	$114 \pm 41$	$110 \pm 19$	$137 \pm 42$
<i>N</i>	1	2	2	3	2

<sup>a</sup> measurement accuracy according to the datasheet (Keithley 2000 6.5 Digit Multimeter).

slipping, thereby enabling all Al layers to conduct. For example, we expect the 9.4 nm thick oxide layers to be above the electron tunneling length and therefore to be nonconductive, even with the present H doping content.<sup>[58]</sup> Hence, we would expect there to be a poorer conductivity for the 50/9.4 sample than the 50/1 cycle or 150 counterparts.

### 3.3.2. Resistance Decrease

Upon initial loading, all samples experience a resistance drop, causing the  $R/R_0$  curves to fall below the theoretical resistance increase (constant volume approximation,<sup>[43]</sup> green line, Figure 3a–e, top). This drop is present in all cases. For better comparison, the initial loading section of all samples is shown in **Figure 6**. Sharp peaks in the signal stem from instrumentation (stage rotation for  $\sin^2\psi$  measurements) and are not

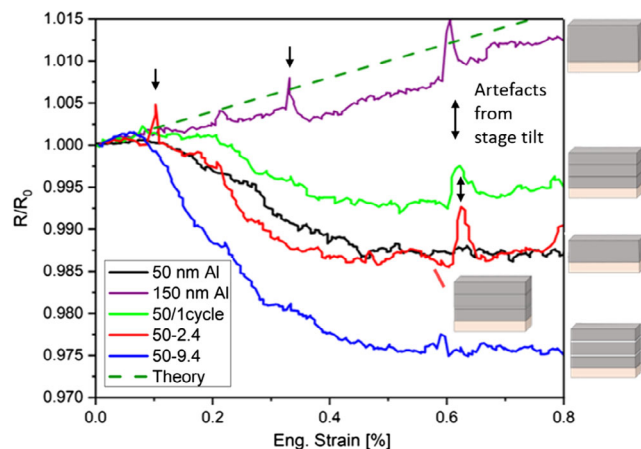


**Figure 6.** Resistance ratio  $R/R_0$  as a function of applied strain and multilayer architecture. Up to 0.5% strain, resistance recovery is observed, which is more pronounced for thinner films and multilayers. Pronounced resistance peaks (black arrows) are artifacts from stage tilting.

representative of thin-film behavior. Compared to stress measurements (central area, diameter 300  $\mu\text{m}$ ), the resistance signal is sampling a larger area ( $\approx 5 \times 20 \text{ mm}$ ) and is therefore affected more by overall sample quality across the whole tensile specimen (surface scratches on the polymer surface prior to deposition, damage/scratches during sample handling). Despite the resulting scatter of individual resistance curves of the same thin-film material,<sup>[59]</sup> the resistance drop of Al upon initial straining is reproducible on various samples and test setups.

Depending on the thin-film architecture, the resistance drop, occurring within the first 0.5% of applied strain, is more or less pronounced. The largest decrease is observed for the 50/9.4 multilayer sample, while the 150 nm Al reference (highest surface roughness, Figure 4a) shows almost no decrease in resistance. For fatigue experiments a decrease in electrical resistance of Cu thin films (initially bimodal grain size: 1.5  $\mu\text{m}$  and ultra-fine grained (UFG) <300 nm; 50% surface fraction each) during the first 1000–2000 cycles has been correlated to strain-induced grain coarsening at the expense of the UFG grain fraction,<sup>[60]</sup> which is not conceivable for monotonic loading. Studies by Haque and coworkers report the role of mechanical strain on the electrical conductivity of aluminum thin films (125 nm), with an average grain size (50 nm; comparable to our films) three times larger than the mean free path of electrons in the material.<sup>[61,62]</sup> Their results show that electrical conductivity is strongly affected by mechanical strain at length scales where dislocation-based deformation mechanisms cease to exist. Contrary to our findings, these studies report an increase in the electrical resistivity ( $\approx 26$ –32%) as a function of applied tensile strain (strain range 0–0.25%,<sup>[61]</sup> 0–0.8%<sup>[62]</sup>).

Using a specific repetitive loading protocol, detailed in the (Section S2, Supporting Information), the origin of the resistance drop during monotonic straining has been investigated thoroughly. It can be concluded that it is a consequence of the way our samples are gripped during straining, such that gradual removal/breaking of a native surface oxide layer under the tensile grips yields better electrical contact. This is in line with reported resistance curves of Al-bilayers on polyimide using a similar clamping system.<sup>[63]</sup> Importantly, the magnitude of the resistance drop is found to be proportional to the initial gauge length (Figure S2, Supporting Information), which is constant ( $L_0 = 23.1 \pm 0.1 \text{ mm}$ ) for the samples shown in Figure 6. Therefore, the gripping effect cannot fully explain the role of sublayer architecture observed in this study, which points toward the layer structure and interfaces between individual Al sublayers as additional influencing factors, since the native oxide layer is identical for the investigated systems, except 150 nm Al considering surface roughness.

### 3.3.3. Electrical Failure and Resistance at Maximum Applied Strain

Despite a similar crack pattern, the sample with 1 ALD cycle exhibits better electrical behavior compared to 2.4 nm oxide layers. Fundamentally, this difference must be due to a lower number of partial or full, tensile-induced cracks, which is suggested by the FIB cross-sections (Figure 5c,d), but not easily quantifiable in a statistically meaningful way. The recorded

resistance is a good alternative way to characterize the crack pattern, more easily accessible than a statistically meaningful crack count.<sup>[39]</sup> To better quantify the difference in the electrical behavior between 2.4 nm and 1 ALD cycle oxide layers, the two electrically characteristic values of 10% deviation from  $R_0$  and  $R/R_0$  at the maximum applied strain (12%) (Table 1) have been analyzed. Indeed, the statistical significance of the  $R/R_{0\text{ max}}$  of 50/2.4 being different from that of 50/1cycle was verified ( $p = 0.012$ ) using a two-tail  $t$  test with equal variances based on a  $p < 0.05$  criterion. In contrast, for 150 nm Al film versus 50/1cycle, no statistically significant difference could be confirmed ( $p = 0.313$ )—requiring an unequal variances test due to the low spread of the 150 nm data. Similarly, 50/2.4 was significantly different from 150 nm Al ( $p = 0.011$ ). The 9.4 nm oxide layer sample was significantly different from all other samples ( $p = 0.027, 0.028, \text{ and } 0.030$  for 150 nm Al, 50/1 cycle, and 50/2.4 respectively). For the 10% resistance increase failure criterion, a statistically significant difference can only be ascertained between 50/2.4 and 50/9.4 ( $p = 0.013$ ) and 150 nm Al and 50/9.4 ( $p = 0.05$ ), due to the relatively high standard deviation of the 50/1 cycle sample.

Further correlation of the crack pattern to the resistance increase using, for instance, the model proposed in ref. [39] is not possible, since it assumes that all cracks are through-thickness such that no current can flow through a crack. While this is true for the reference samples, the multilayers also exhibit isolated sublayer fracture of the bottom or bottom and top layer, even up to a total applied strain of 12%. Hwang et al.<sup>[21]</sup> showed similar sublayer cracking and crack deflection in Cu/graphene (Gr) multilayers after cyclic bending. Bending fatigue cracks are expected to start in the topmost layer, subjected to the largest tensile bending strain, and deflected at the Cu/Gr interface due to the high strength and modulus of the graphene; the maximum crack size being limited to the repeat layer spacing of Cu is further hindering crack propagation. In our case of monotonic tensile testing of Al/Al<sub>2</sub>O<sub>3</sub> multilayer, the crack initiation sites cannot be identified unambiguously, yet the middle layer appears to be most crack resistant, even with 9.4 nm oxide layers. Since our oxide layers are expected to remain electrically conductive up to 2–3 nm,<sup>[64,65]</sup> electrons are able to bypass cracked Al sublayers making the 50/1cycle and 5/2.4 multilayers particularly promising examples of electrically robust materials for flexible electronics applications.

### 3.4. Electromechanical Behavior

The electrical, mechanical, and post-mortem SEM analysis correlates well in terms of thin-film deformation mechanisms. Important electrical and mechanical parameters are summarized in Table 1 as a function of multilayer architecture. Conceptually, the 50/1 cycle sample with discontinuous Al<sub>2</sub>O<sub>3</sub> layers is located between the reference Al films and the Al/Al<sub>2</sub>O<sub>3</sub> multilayers. To understand the electromechanical behavior as a function of layer architecture, it is interesting to focus first on the behavior of the pure Al films (50, 150, 50/1 cycle) in the tensile direction. Compared to the stress plateau of perfectly ductile thin films (Cu<sup>[45]</sup>) all reference Al films show a slight stress decrease during loading after reaching the elastic limit. As expected, we observed

an increase in initial resistance  $R_0$ , an increase in maximum stress<sup>[26,45]</sup>, and a reduction of electrical failure strain<sup>[66–68]</sup> for decreasing film thickness and grain size between 150 nm and 50 nm Al. The maximum film stress of the 50/1 cycle Al sample, with 50 nm Al sublayers separated by 1 ALD cycle (0.14 nm Al<sub>2</sub>O<sub>3</sub>) is lower compared with the 50 nm film and slightly higher compared with 150 nm Al. The strengthening trend visible in Figure 3 becomes slightly reduced when taking the average of multiple measurements.

To analyze the strengthening behavior, we can consider the different percentages and types of interfaces and free surfaces for the three different cases. Although a good approximation for grain geometry would be hexagonal prisms, we model the Al grains here as cubes for simplicity, without loss of interpretability. With this, we can distinguish between Al–Al grain boundaries, the metal–polymer interface, and natural or artificial oxide interfaces, as schematically shown in Figure 7.

For a cubic Al grain in the 50 and 150 nm Al film 1/6 of the total grain boundaries are with the polymer interlayer, and 1/6 are native oxide interfaces (surface). Both of these types are interfaces with an amorphous phase. Al–Al grain boundaries constitute the remaining 2/3 (1/3 lateral and 1/3 in loading direction). In the rest of the following discussion, the 150 nm Al film is not considered to avoid straightforward grain-size-based strength arguments. In multilayers, the total number of Al–Al grain boundaries is systematically increased. For 50/1 cycle, we are assuming that all additional boundaries are Al–Al, despite having 1 cycle ALD, which is enough to interrupt the Al grain growth. Therefore, this type is not a simple Al–Al grain boundary, though is categorized here as such. Following this assumption, in the 50/1 cycle architecture, only 1/18 of grain boundaries are with the amorphous polymer interlayer, and similarly 1/18 with the native oxide. Furthermore, the proportion of Al–Al grain boundaries along the loading direction remain constant.

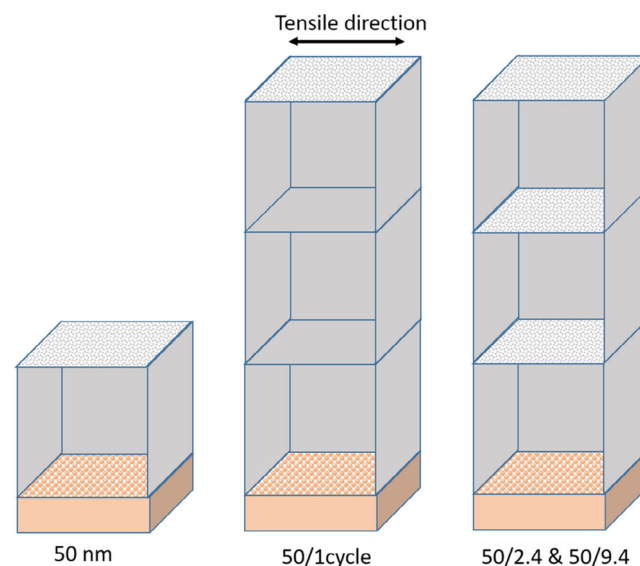


**Figure 7.** Schematic representation of grain boundary types presents in the thin films, assuming cubic Al grains. The three different types include Al–Al grain boundaries, the metal–polymer interface, and natural or artificial oxide interfaces.



The percentages of boundary types as a function of film architecture, assuming cubic grains and noting the layer thickness and in-plane grain width given in Section 2.1, are summarized in Table 2.

Since the 50 nm Al film is stronger compared to the 50/1 cycle counterpart, we can conclude that the free surface is an inefficient location for dislocation nucleation, or a poor sink. This phenomenon is well known in the literature from works on 0D nanoparticle and core-shell structures (Au on Ag), where the addition of a shell results in softening as nucleation sources at the Ag grain surface is stimulated by the Au layer.<sup>[69]</sup> In our case, we are simply covering the free surface with the self-same material rather than a second phase. In contrast, works from Gruber et al. on ultra-thin Cu films with and without passivation layers show how a Ta capping layer can strengthen the Cu.<sup>[45]</sup> One should note that Ta is considerably stronger than Cu, unlike Al on Al here.

The observed strength difference between 50 nm Al (stronger) and 50/1 cycle Al (weaker) also importantly indicates that the polymer interface is not the weakest link in nucleating dislocations: the presence of Al-Al grain boundaries has a greater softening effect than the Al-PI interface.

Introducing oxide layers has a significant impact on electro-mechanical behavior. For both Al/Al<sub>2</sub>O<sub>3</sub> multilayers, 27.8% of the interfaces are oxides. With increasing oxide layer thickness from 2.4 to 9.4 nm, a clear strengthening of the Al sublayers is observed as the measured maximum film stress,  $\sigma_{\max}$ , increases and shifts to slightly higher applied strains. This gain in strength comes however at the cost of ductility upon further loading. With the thickest oxide layers, a clear transition in the thin-film failure mechanism is observed. This is consistently reflected in the parallel and perpendicular film stress evolution (pronounced stress peaks), the recorded resistance signal (steep increase and shift of the electrical failure to lower applied strains), and the morphology of the crack pattern developing on the surface (long straight cracks). Early fragmentation of ductile films in multilayers with pronounced through-thickness cracking, similar to the 50/9.4 film, has been observed with other in situ XRD experiments,<sup>[26,27,46,70]</sup> the reason for embrittlement being stress concentration at fracture sites of brittle layers.<sup>[26,27]</sup> Therefore, cracking of the Al layers in the 50/9.4 sample can likely be ascribed to fracture of the 9.4 nm oxide layers happening concurrently or before the Al fracture is observed at around 2% applied strain.

When the oxide layer thickness is reduced to 2.4 nm, the film stress peak and particularly stress relaxation, leveling around 200 MPa rather than zero film stress, are less pronounced. The crack pattern developing on the surface is similar to the Al reference films in terms of crack morphology and spacing

**Table 2.** Percentage of boundary types for the different 50 nm based reference and multilayer films assuming cubic Al grains.

Architecture	Natural (or artificial) oxide interface [%]	Polymer interlayer [%]	Al-Al grain boundary [%]
50	16.7 (0)	16.7	66.7
50/1cycle	5.6 (0)	5.6	88.9
50/2.4 and 50/9.4	5.6 (22.2)	5.6	66.7

(Figure 4a–d), indicating that the deformation of the Al sublayers with 2.4 nm oxides is still dominated by the Al layers themselves. Two scenarios are plausible to explain why no embrittlement is observed in this case: either: 1) fracture of the thinner oxides happens at much higher applied strains as compared to deformation of the Al sublayers due to structural perfection and low defect density or 2) fracture occurs but the stress concentration at the fracture sites is not high enough to cause fragmentation of adjacent Al sub-layers. From the experimental data, it cannot be determined with certainty which one is the case, as the deformation of the oxide layers cannot be traced directly with the presented XRD and post-mortem SEM approach.

The literature shows that ultrathin amorphous Al<sub>2</sub>O<sub>3</sub> layers can be extremely strong and ductile, providing a perfect structure and the absence of geometrical defects. Oxide layer thickness is often identified as the limiting factor for structural perfection and ductility. In micro-pillar compression experiments of similar Al/Al<sub>2</sub>O<sub>3</sub> structures, where the oxide layers are loaded in biaxial tension by the expanding Al layers, cracking of the oxide layers has been observed at thicknesses above or equal to 5 nm,<sup>[7]</sup> which is in line with the differences observed between 2.4 and 9.4 nm in the current study. Frankberg et al. showed how 40 nm thick, amorphous, pulsed laser deposited (PLD) Al<sub>2</sub>O<sub>3</sub> can deform up to 15% strain in tension without fracture at room temperature and high strain rate by a viscous creep mechanism.<sup>[20]</sup> PLD results in an extremely low hydrogen content in the film, which could be one reason for the observed difference in performance, as we can clearly link the failure of the 50/9.4 film to the fracture of the 9.4 nm oxide layers. Our ALD deposition at 120 °C yields an H content of 10%.<sup>[71]</sup> While deposition at higher temperatures is known to reduce the H content of the ALD film,<sup>[71]</sup> this is not a practical solution for a multilayer containing Al due to grain growth during deposition and deterioration of the polymer substrate. As a future alternative, plasma-enhanced ALD is known to result in low H contents<sup>[71]</sup> even for deposition at RT. Furthermore, the position of the oxides within our multilayers could reduce their fracture resistance. In this regard, Cordill et al. recently showed that the layer order and position of the brittle component in a multilayer strongly influence its fracture behavior, highlighting the beneficial role of close proximity to the polymer substrate.<sup>[34]</sup> The fact that our oxide films are not directly interfacing with the polymer substrate could contribute to their potential mechanical weakening.

Regarding the unloading behavior, very little recovery of the electrical resistance is observed in all cases. The recovery is linear and parallel to the constant volume approximation. Missing resistance recovery can be ascribed to the oxidation of crack edges, with the native oxide being non-conductive. Additionally for the multilayers, crack closure on sublayers can be prohibited by adjacent intact ones, as FIB/SEM analysis after unloading shows that sub-layer cracks are open, whereby preferential FIB induced damage at pre-existing cross-sectional defects needs to be considered. Certainly for the thickest oxide case cracks are visibly open in top view, even though they do not continuously penetrate all Al sublayers after straining to 12%. This yields a particularly high final resistance ratio  $((R/R_0)_{\text{End}} = 12.5$  with  $(R/R_0)_{\text{max}} = 13.5$ ) in comparison to noble metal thin films (50 nm Au embrittled with 10 nm Cr,  $(R/R_0)_{\text{End}} = 5$ , despite  $(R/R_0)_{\text{max}} = 20$ ).<sup>[28,72]</sup>

The improved electromechanical damage tolerance of multilayers with thinner oxide layers within the applied strain range is indisputable. For this discussion, the 150 nm Al film can serve as a perfect example of ductile electromechanical behavior parallel and perpendicular to the straining direction. While the film stress data of the thinner Al film is less interpretable due to the weaker XRD signal, the fact that stress peaks are observed in both directions amplifies the credibility of the measurements. For ductile thin films, this embrittlement as a function of decreasing film thickness is well understood.<sup>[66]</sup> Both the film stress and resistance evolutions of the 50/1 cycle film indicate that a single ALD cycle did not cause significant embrittlement, even compared to the 150 nm Al film in the longitudinal direction. Even without significant strengthening effects at this point, sub-layering can be beneficial for through-thickness damage tolerance or functional properties. Only with 9.4 nm thick oxide layers is significant embrittlement observed. The trend in our data fits into the bigger picture of length-scale-dependent deformation of brittle/ductile multilayers and substantially extends the range of multilayer thickness modulation ratios accessed thus far. In **Figure 8**, our multilayer film systems have been added (symbol size corresponding to achieved maximum strength) into a map of possible layer thickness combinations (modulation period  $\lambda = t_{\text{brittle}} + t_{\text{ductile}}$  and modulation ratio  $\eta = t_{\text{brittle}}/t_{\text{ductile}}$ ,<sup>[30]</sup>  $t$  is equal to the film thickness), also including the existing literature data. In the previously studied regime (dark blue region), preservation of ductile deformation was reported by Wu et al.<sup>[30]</sup> in a small parameter region with  $\eta < 0.2$  and  $\lambda = 40 \pm 20$  nm (yellow region), whereby the brittle-to-ductile

transition is characterized by a fracture toughness criterion, as further detailed in ref. [30]. For clarity, data points of the original graph have been removed, showing only the outline of the ductile fracture regime. By including ALD combined with PVD without breaking the vacuum, the whole region highlighted in dashed green is now accessible. Importantly, this allows us to now access the area directly below the previously identified beneficial ductile regime (exemplarily outlined with yellow lines in Figure 8) for the first time and our films showcase its large potential for ductile multilayers. The dashed borders to the physically inaccessible region in red and the previously accessible via PVD region in light blue are drawn based on the following assumptions: a minimum PVD thickness of 3 nm for continuous films and 0.2 nm as the conservative lower thickness limit of an ALD layer, considering the approximate thickness of metal or binary compound monolayers.<sup>[73]</sup> The overlap between our PVD/ALD area (green) and the previously reported PVD results (dark blue) is a result of our assumption of the minimum achievable PVD thickness as 3 nm, while the study in ref. [30] reports a minimum PVD layer thickness of 1 nm; this is heavily dependent on the deposited element and sputter conditions.<sup>[74,75]</sup>

#### 4. Conclusion

Uniaxial tensile straining with in situ XRD film stress measurement parallel and perpendicular to the tensile direction, as well as four-point probe resistance measurements was performed on unique Al/Al<sub>2</sub>O<sub>3</sub> multilayers (magnetron sputtering/ALD) and Al reference films on flexible polyimide substrates. Ultrathin Al<sub>2</sub>O<sub>3</sub> layers are used to interrupt the out-of-plane grain growth of Al, generating Al-sublayer structures with a grain size well below the total film thickness. HR-TEM analyses show that a single ALD cycle (nominally 0.14 nm Al<sub>2</sub>O<sub>3</sub>) is enough to interrupt and restart Al grain growth, yielding distinct but very narrow interfaces to adjacent Al sublayers. In terms of electrical performance under load, no statistically significant difference or deterioration of electrical failure criteria was found for multilayers with 1 ALD cycle as compared to a pure 150 nm Al reference film. Additionally, an amorphous interlayer (thickness  $\approx 5$  nm) between Al and the polymer substrate has been shown for the first time for laboratory magnetron sputter deposition. This specific interface structure is related to the good adhesion and electromechanical behavior. While buckling is not the only criteria for interface quality, the absence of delamination within the investigated strain regime, despite the evolution of significant compressive stresses in the transverse direction in some cases, definitely confirms the good adhesion of our films. Through optimization of the oxide layer thickness, multilayers with improved strength and high lateral and through-thickness damage tolerance can be designed. XRD film stress, electrical resistance, and post-mortem FIB/SEM data are in good agreement regarding the deformation of Al sublayers as a function of Al<sub>2</sub>O<sub>3</sub> layer thickness. Strengthening of Al sublayers is observed with increasing oxide thickness. For multilayers with 9.4 nm Al<sub>2</sub>O<sub>3</sub> layers (67 ALD cycles) embrittlement and imposed fracture of Al sublayers occurs around 2% applied strain, resulting in stress relaxation and the evolution of long straight cracks. With 2.4 nm oxides (17 ALD cycles) the multilayers show improved damage tolerance, where the crack

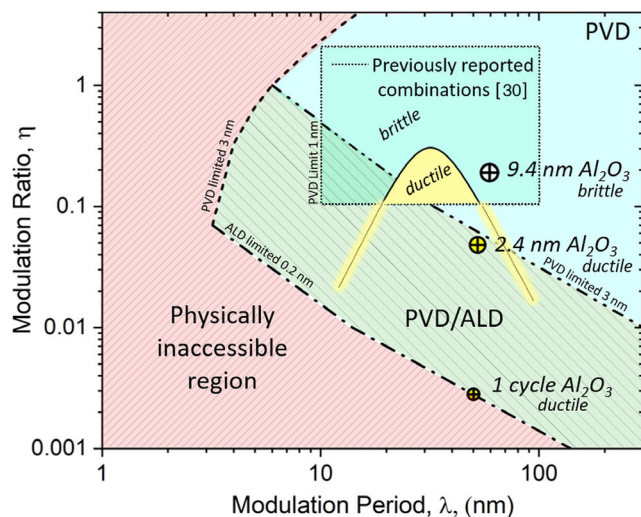


**Figure 8.** Length-scale dependent deformation of brittle–ductile multilayer thin films. Different colored regions correspond to previously accessible through physical vapor deposition (PVD, light blue), previously reported PVD (light blue and yellow), newly accessible through atomic layer deposition (ALD)/PVD (hashed green), and physically inaccessible region (hashed red). Dashed lines are drawn based on a conservative estimate for achievable individual layer thicknesses of 3 nm/0.2 nm for PVD/ALD, respectively, while the previously investigated area reports a minimum PVD layer thickness of 1 nm. Our data points have been added with symbol diameter according to the measured film strength. Data in the dotted rectangle has been taken from Ref. [30].

morphology and spacing are similar to the ductile reference Al films, constituting the best compromise for strength and ductility within the investigated oxide thickness regime. Quite possibly there is room for further optimization of oxide layer thickness within the range of 0.14–2.4 nm, to achieve the maximum in terms of Al strength and ductility. Importantly, all multilayers exhibit a certain degree of sublayer fracture, with adjacent Al layers remaining intact even after straining to 12%, while all cracks in the reference Al films are through-thickness. In summary, the combined ALD/PVD approach offers great potential to study length-scale dependent multilayer deformation mechanisms over the large thickness and modulation ratios and, in particular, uniquely access and extend areas close to previously identified regions of beneficial ductile deformation in search of damage-tolerant thin-film materials. Similarly, microstructural engineering of thin films with unique mechanical and functional properties resulting from sublayer architectures in the nm range can be achieved for innovative flexible and rigid thin-film applications.

## 5. Experimental Section

**Synthesis of ALD/PVD Multilayers and Reference Thin Films:** Multilayers of Al (50 nm) and Al<sub>2</sub>O<sub>3</sub> (0.14–9.4 nm) were deposited onto 50 μm thick polyimide (PI, Upilex-S) and Si substrates through alternating cycles of magnetron sputtering (PVD) and ALD without breaking vacuum. The combined ALD/PVD deposition chamber is described in detail in ref. [6]. Polymer substrates were pre-cut into an array of tensile stripes (6 mm × 40 mm). Prior to deposition the substrates were ultrasonically cleaned and kept at elevated temperatures (≈8 h, 100 °C, UHV) during the pre-heating of the ALD process. Likewise, substrates for reference films of pure Al without ALD were also pre-heated. This heating facilitated the columnar growth of Al grains. Al was magnetron sputtered from two targets (purity 99.9%) equidistant from the substrate table without substrate rotation. Sputter parameters include a current of 150 mA, a base pressure of  $7 \times 10^{-7}$  mbar, a working pressure of  $5 \times 10^{-3}$  mbar (Ar), and a combined deposition rate of 0.05 nm s<sup>-1</sup> from two targets. ALD of Al<sub>2</sub>O<sub>3</sub> was performed at 120 °C with a precursor sequence of pulse-exposure-purge at 0.5–1–100 s for trimethylaluminum (TMA) and 0.5–1–150 s for H<sub>2</sub>O. Precursors were kept at room temperature, with Ar used as the carrier and purging gas. The deposition conditions resulted in amorphous and stoichiometric Al<sub>2</sub>O<sub>3</sub> with a growth per cycle of approximately 0.14 nm/cycle as reported in ref. [6]. The following nominal oxide thicknesses were achieved by adjusting the number of ALD cycles: 67 cycles – 9.4 nm, 17 cycles – 2.4 nm, 1 full cycle – 0.14 nm. Three Al/Al<sub>2</sub>O<sub>3</sub> multilayers were fabricated: 50/9.4/50/9.4/50, 50/2.4/50/2.4/50, 50/1cycle/50/1cycle/50 (thickness in nm), referred to as 50/9.4, 50/2.4 and 50/1cycle, respectively, throughout the manuscript, along with 50 nm and 150 nm Al reference films. FIB (FEI Helios NanoLab Dualbeam, USA) prepared lift outs were investigated with TEM (Jeol JEM 2200 fs, Japan). Thicknesses and microstructure of individual PVD layers were confirmed via bright field scanning cross-sectional imaging (BF-STEM). For ALD layers, high resolution cross-sectional imaging (HR-TEM) was performed.

**In situ Electro-Mechanical Characterization:** XRD (synchrotron radiation, KMC-2 beamline,<sup>[76]</sup> BESSY II, Berlin) and sin<sup>2</sup>ψ analysis<sup>[77]</sup> were used to measure longitudinal and transversal (parallel and perpendicular to the tensile direction, respectively) Al lattice strains in situ during continuous uniaxial straining of the film–polymer couple (Anton Paar TS600, maximum strain  $\epsilon_{\max} = 12\%$ , 3 min hold period at  $\epsilon_{\max}$ , gauge length =  $22.9 \pm 0.2$  mm, displacement rate = 0.1 mm min<sup>-1</sup>, strain rate  $8 \times 10^{-5}$ /s). Resistance probes were incorporated into the grips of the straining stage in a similar manner as presented in ref. [43]. A total of two samples were tested for each multilayer and reference geometry. The 111 Bragg peak of Al was recorded in reflection geometry with a Bruker VANTEC 2000 area detector with an exposure time of 9 s, a X-ray wavelength of 0.154 nm, and a beam diameter of 300 μm. Before and after each tensile test residual lattice strains

were measured with high resolution at 11 different ψ angles. In situ measurements were performed at 5 different ψ angles. The ψ range for both cases was between 0 and 45 degrees. A Pearson fit was applied to determine peak positions and peak widths. Film stresses were calculated using X-ray elastic constants (XECs) ( $1/2 S_2 = 1.8436$ ) for 111 Al reflections.<sup>[77]</sup> XECs were calculated from single-crystal elastic constants assuming the Hill model with the software ElastiX.<sup>[78]</sup> No XRD signal was obtained for the amorphous oxide layers. All samples were examined post-mortem with SEM (Hitachi S-4800, Japan). Cross-sectional FIB cuts (Zeiss Auriga FIB-SEM, milling current 100 pA, SEM voltage 7 kV) were used to identify the through-thickness crack propagation.

## Supporting Information

Supporting Information is available from the Wiley Online Library or from the author.

## Acknowledgements

HZB is gratefully acknowledged for the allocation of synchrotron radiation beamtime and financial support (192-08532ST, 202-09765ST). B.P. and T.E.J.E. would like to acknowledge support from the EMPAPOSTDOCS-II program, which received funding from the European Union's Horizon 2020 research and innovation program under the Marie Skłodowska-Curie grant agreement number 754364. T.E.J.E. acknowledges funding from the European Union's Horizon 2020 research and innovation programme under the Marie Skłodowska-Curie grant agreement No. 840222. The authors acknowledge further funding from the Austrian Science Fund (FWF, Nanofilm, Project I 4913-N).

## Conflict of Interest

The authors declare no conflict of interest.

## Data Availability Statement

The data that support the findings of this study are available from the corresponding author upon reasonable request.

## Keywords

amorphous oxides, cracking, mechanical properties, multilayer thin films, tensile test

Received: June 29, 2022

Revised: November 7, 2022

Published online:

- [1] J. Wang, K. Kang, R. F. Zhang, S. J. Zheng, I. J. Beyerlein, N. A. Mara, *JOM* **2012**, *64*, 1208.
- [2] S. M. Kim, W. Kim, Y. Hwangbo, J. H. Kim, S. M. Han, *2D Mater.* **2019**, *6*, 045051.
- [3] K. K. Shih, D. B. Doce, *Appl. Phys. Lett.* **1992**, 654.
- [4] D. Bhattacharyya, N. A. Mara, P. Dickerson, R. G. Hoagland, A. Misra, *Philos. Mag.* **2010**, *90*, 1711.
- [5] G. Abadias, F. Pailloux, S. N. Dub, *Surf. Coat. Technol.* **2008**, *202*, 3683.
- [6] T. Xie, T. E. J. Edwards, N. M. della Ventura, D. Casari, E. Huszár, L. Fu, L. Zhou, X. Maeder, J. J. Schwiedrzik, I. Utke, L. Pethő, J. Michler, *Thin Solid Films* **2020**, *711*, 138287.



- [7] T. E. J. Edwards, T. Xie, N. M. della Ventura, D. Casari, C. Guerra, E. Huszar, X. Maeder, J. J. Schwiedrzik, I. Utke, L. Pethö, J. Michler, *Acta Mater.* **2022**, 240, 118345.
- [8] Y. Kim, J. Lee, M. S. Yeom, J. W. Shin, H. Kim, Y. Cui, J. W. Kysar, J. Hone, Y. Jung, S. Jeon, S. M. Han, *Nat. Commun.* **2013**, 4, 2114.
- [9] I. Salehinia, S. Shao, J. Wang, H. M. Zbib, *JOM* **2014**, 66, 2078.
- [10] M. Ben Daia, P. Aubert, S. Labdi, C. Sant, F. A. Sadi, P. Houdy, J. L. Bozet, *J. Appl. Phys.* **2000**, 87, 7753.
- [11] S. Lotfian, C. Mayer, N. Chawla, J. Llorca, A. Misra, J. K. Baldwin, J. M. Molina-Aldareguía, *Thin Solid Films* **2014**, 571, 260.
- [12] J. L. He, W. Z. Li, H. D. Li, C. H. Liu, *Surf. Coat. Technol.* **1998**, 103, 276.
- [13] N. Li, X. Y. Liu, *J. Mater. Sci.* **2018**, 53, 5562.
- [14] S. Pathak, N. Li, X. Maeder, R. G. Hoagland, J. K. Baldwin, J. Michler, A. Misra, J. Wang, N. A. Mara, *Scr. Mater.* **2015**, 109, 48.
- [15] S. A. Barnett, A. Madan, *Scr. Mater.* **2004**, 50, 739.
- [16] L. W. Yang, C. Mayer, N. Chawla, J. Llorca, J. M. Molina-Aldareguía, *Philos. Mag.* **2016**, 96, 3336.
- [17] S. B. Sinnott, E. C. Dickey, *Mater. Sci. Eng., R* **2003**, 43, 1.
- [18] J. Wang, A. Misra, *Curr. Opin. Solid State Mater. Sci.* **2014**, 18, 19.
- [19] P. M. Anderson, C. Li, *Nanostruct. Mater.* **1995**, 5, 349.
- [20] E. J. Frankberg, J. Kalikka, F. G. Ferré, L. Joly-Pottuz, T. Salminen, J. Hintikka, M. Hokka, S. Koneti, T. Douillard, B. Le Saint, P. Kreiml, M. J. Cordill, T. Epicier, D. Stauffer, M. Vanazzi, L. Roiban, J. Akola, F. Di Fonzo, E. Levänen, K. Masenelli-Varlot, *Science* **2019**, 366, 864.
- [21] B. Hwang, W. Kim, J. Kim, S. Lee, S. Lim, S. Kim, S. H. Oh, S. Ryu, S. M. Han, *Nano Lett.* **2017**, 17, 4740.
- [22] F. Muktepavela, G. Bakradze, E. Tamanis, S. Stolyarova, N. Zaporina, *Phys. Status Solidi C* **2005**, 2, 339.
- [23] A. T. Alpas, J. D. Embury, D. A. Hardwick, R. W. Springer, *J. Mater. Sci.* **1990**, 25, 1603.
- [24] R. W. Revie, *Corrosion and Corrosion Control - An Introduction to Corrosion Science and Engineering*, Wiley **2008**.
- [25] Y. Ding, D. O. Northwood, A. T. Alpas, *Surf. Coat. Technol.* **1993**, 62, 448.
- [26] V. M. Marx, F. Toth, A. Wiesinger, J. Berger, C. Kirchlechner, M. J. Cordill, F. D. Fischer, F. G. Rammerstorfer, G. Dehm, *Acta Mater.* **2015**, 89, 278.
- [27] B. Putz, O. Glushko, V. M. Marx, C. Kirchlechner, D. Toebbens, M. J. Cordill, *MRS Adv.* **2016**, 1, 773.
- [28] B. Putz, R. L. Schoepfner, O. Glushko, D. F. Bahr, M. J. Cordill, *Scr. Mater.* **2015**, 102, 23.
- [29] P. Kreiml, M. Rausch, V. L. Terziyska, J. Winkler, C. Mitterer, M. J. Cordill, *Scr. Mater.* **2019**, 162, 367.
- [30] K. Wu, J. Y. Zhang, J. Li, Y. Q. Wang, G. Liu, J. Sun, *Acta Mater.* **2015**, 100, 344.
- [31] P. A. Gruber, C. Solenthaler, E. Arzt, R. Spolenak, *Acta Mater.* **2008**, 56, 1876.
- [32] J. Lohmiller, N. C. Woo, R. Spolenak, *Mater. Sci. Eng., A* **2010**, 527, 7731.
- [33] M. N. Polyakov, J. Lohmiller, P. A. Gruber, A. M. Hodge, *Adv. Eng. Mater.* **2015**, 17, 810.
- [34] M. J. Cordill, P. Kreiml, B. Putz, D. Faurie, P.-O. Renault, D. Thiaudière, C. Mocuta, *Scr. Mater.* **2021**, 194, 113656.
- [35] G. Geandier, D. Faurie, P. O. Renault, D. Thiaudière, E. Le Bourhis, *J. Appl. Crystallogr.* **2014**, 47, 181.
- [36] D. Faurie, F. Zighem, P. Godard, G. Parry, T. Sadat, D. Thiaudière, P.-O. Renault, *Acta Mater.* **2019**, 165, 177.
- [37] S. Djaziri, P. O. Renault, F. Hild, E. Le Bourhis, P. Goudeau, D. Thiaudière, D. Faurie, *J. Appl. Crystallogr.* **2011**, 44, 1071.
- [38] M. J. Cordill, O. Glushko, J. Kreith, V. M. Marx, C. Kirchlechner, *Microelectron. Eng.* **2014**, 137, 96.
- [39] O. Glushko, B. Putz, M. J. Cordill, *Thin Solid Films* **2020**, 699, 137906.
- [40] D. D. Gebhart, A. Krapf, C. Gammer, B. Merle, M. J. Cordill, *Scr. Mater.* **2022**, 212, 114550.
- [41] J. Wilt, Y. Gong, M. Gong, F. Su, H. Xu, R. Sakidja, A. Elliot, R. Lu, S. Zhao, S. Han, J. Z. Wu, *Phys. Rev. Appl.* **2017**, 7, 1.
- [42] J. Wilt, R. Sakidja, R. Goul, J. Z. Wu, *ACS Appl. Mater. Interfaces* **2017**, 9, 37468.
- [43] O. Glushko, M. J. Cordill, *Exp. Tech.* **2014**, 40, 1.
- [44] P. Kreiml, M. Rausch, V. L. Terziyska, H. Köstenbauer, J. Winkler, C. Mitterer, M. J. Cordill, *Thin Solid Films* **2018**, 665, 131.
- [45] P. A. Gruber, J. Böhm, F. Onuseit, A. Wanner, R. Spolenak, E. Arzt, *Acta Mater.* **2008**, 56, 2318.
- [46] P. A. Gruber, E. Arzt, R. Spolenak, *J. Mater. Res.* **2009**, 24, 1906.
- [47] S. Frank, U. A. Handge, S. Olliges, R. Spolenak, *Acta Mater.* **2009**, 57, 1442.
- [48] O. Kraft, M. Hommel, E. Arzt, *Mater. Sci. Eng., A* **2000**, 288, 209.
- [49] L. P. H. Jeurgens, W. G. Sloof, F. D. Tichelaar, E. J. Mittemeijer, *J. Appl. Phys.* **2002**, 92, 1649.
- [50] E. Langereis, S. B. S. Heil, H. C. M. Knoop, W. Keuning, M. C. M. Van De Sanden, W. M. M. Kessels, *J. Phys. D: Appl. Phys.* **2009**, 42, 073001.
- [51] A. A. Taylor, M. J. Cordill, L. Bowles, J. Schalko, G. Dehm, *Thin Solid Films* **2013**, 531, 354.
- [52] B. Putz, G. Milassin, Y. Butenko, B. Völker, C. Gammer, C. Semprinoschnig, M. J. Cordill, *Surf. Coat. Technol.* **2017**, 332, 368.
- [53] B. Putz, G. Milassin, Y. Butenko, B. Völker, C. Gammer, C. Semprinoschnig, M. J. Cordill, *Surf. Interface Anal.* **2018**, 50, 579.
- [54] S. H. Oh, C. Rentenberger, J. Im, C. Motz, D. Kiener, H. P. Karnthaler, G. Dehm, *Scr. Mater.* **2011**, 65, 456.
- [55] M. J. Cordill, F. D. Fischer, F. G. Rammerstorfer, G. Dehm, *Acta Mater.* **2010**, 58, 5520.
- [56] T. Jörg, M. J. Cordill, R. Franz, C. Kirchlechner, D. M. Töbrens, J. Winkler, C. Mitterer, *Mater. Sci. Eng., A* **2017**, 697, 17.
- [57] L. Atanasoska, S. G. Anderson, H. M. Meyer III, Z. Lin, J. H. Weaver, *J. Vac. Sci. Technol., A* **1987**, 5, 3325.
- [58] M. A. Botzakaki, G. Skoulatakis, N. Xanthopoulos, V. Gianneta, A. Travlos, S. Kennou, S. Ladas, C. Tsamis, E. Makarona, S. N. Georga, C. A. Krontiras, *J. Vac. Sci. Technol., A Vac. Surf. Film* **2018**, 36, 01A120.
- [59] B. Putz, *PhD Thesis*, Univ. Leoben, Leoben, Austria **2017**.
- [60] O. Glushko, M. J. Cordill, *JOM* **2014**, 66, 598.
- [61] H. F. Lee, S. Kumar, M. A. Haque, *Acta Mater.* **2010**, 58, 6619.
- [62] S. Kumar, D. Garcia, J. Jin, A. Haque, *J. Vac. Sci. Technol. B* **2015**, 33, 022002.
- [63] B. Putz, B. Völker, C. Semprinoschnig, M. J. Cordill, *Microelectron. Eng.* **2017**, 167, 17.
- [64] E. J. Patiño, N. G. Kelkar, *Appl. Phys. Lett.* **2015**, 107, 1.
- [65] V. D. Das, M. S. Jagadeesh, *Phys. Status Solidi* **1981**, 66, 327.
- [66] R. M. Niu, G. Liu, C. Wang, G. Zhang, X. D. Ding, J. Sun, *Appl. Phys. Lett.* **2007**, 90, 2007.
- [67] N. Lu, X. Wang, Z. Suo, J. Vlassak, *J. Mater. Res.* **2009**, 24, 379.
- [68] N. Lu, Z. Suo, J. J. Vlassak, *Acta Mater.* **2010**, 58, 1679.
- [69] A. Sharma, J. Amodeo, N. Gazit, Y. Qi, O. Thomas, E. Rabkin, *ACS Nano* **2021**, 15, 14061.
- [70] B. Putz, C. May-Miller, V. Matl, B. Völker, D. M. Töbrens, C. Semprinoschnig, M. J. Cordill, *Scr. Mater.* **2018**, 145, 5.
- [71] C. Guerra-Nunez, M. Döbeli, J. Michler, I. Utke, *Chem. Mater.* **2017**, 29, 8690.
- [72] B. Putz, O. Glushko, V. M. Marx, C. Kirchlechner, D. M. Toebbens, M. J. Cordill, *MRS Adv.* **2016**, 773.

- [73] M. Ylilammi, *Thin Solid Films* **1996**, 279, 124.
- [74] M. Kawamura, T. Mashima, Y. Abe, K. Sasaki, *Thin Solid Films* **2000**, 377–378, 537.
- [75] M. Ohring, *The Materials Science of Thin Films*, Academic Press, San Diego, CA, USA **1992**.
- [76] D. Töbrens, S. Zander, J. *Large-Scale Res. Facil.* **2016**, 2, 1.
- [77] I. C. Noyan, J. B. Cohen, *Residual Stress: Measurement by Diffraction and Interpretation*, Springer, New York, NY **1987**.
- [78] H. Wern, N. Koch, T. Maas, *Mater. Sci. Forum* **2002**, 404–407, 127.